PERGAMON

Renewable Energy 21 (2000) 1–22

RENEWABLE ENERGY

www.elsevier.com/locate/renene

Design and optimisation of a combination solar collector–thermal engine operating on Mars

Viorel Badescu[a,*], Gheorghe Popescu[b], Michel Feidt[c]

[a] *"Candida Oancea" Institute of Solar Energy, Faculty of Mechanical Engineering, Polytechnic University of Bucharest, Spl. Independenţei 313, 77206, Bucharest, Romania*

[b] *Applied Thermodynamics Department, Faculty of Mechanical Engineering, Polytechnic University of Bucharest, Spl. Independenţei 313, 77206, Bucharest, Romania*

[c] *L.E.M.T.A., University "H. Poincare" of Nancy 1, UMR CNRS No. 7563, 2 Avenue de la Foret de Haye, 54516, Vandoeuvre-les-Nancy, France*

Received 16 November 1999; accepted 29 November 1999

Abstract

A "dynamic" solar power plant (which consists of a solar collector–thermal engine combination) is proposed as an alternative for the more usual photovoltaic cells. A model for heat losses in a selective flat-plate solar collector operating on Mars is developed. An endoreversible Carnot cycle is used to describe heat engine operation. This provides upper limits for real performances. The output power is maximized. Meteorological and actinometric data provided by Viking Landers are used as inputs. Two strategies of collecting solar energy were considered: (i) horizontal collector; (ii) collector tilt and orientation are continuously adjusted to keep the receiving surface perpendicular on the Sun's rays. The influences of climate and of various design parameters on solar collector heat losses, on engine output power and on the optimum sun-to-user efficiency are discussed. © 2000 Elsevier Science Ltd. All rights reserved.

Keywords: Flat plate collector; Thermal engine; Mars

* Corresponding author. Tel.: +40-1-410-0400, ext 339; fax: +40-1-410-4488.
E-mail address: badescu@theta.termo.pub.ro (V. Badescu).

0960-1481/00/$ - see front matter © 2000 Elsevier Science Ltd. All rights reserved.
PII: S0960-1481(99)00129-9

1. Introduction

A variety of future space initiatives as missions on the Moon and Mars and orbiting stations require the availability of power generation units with capacities ranging from about 1 kW to many MW utilizing chemical energy, radio-isotopes, solar radiation or nuclear fission as primary energy source [1,2]. The utilization of systems, which use internally stored nuclear and chemical energy, implies in many cases limited life and excessive weight. Properly designed solar power systems can offer long life in space.

Among various solar technologies a leading position is played by the photovoltaic (PV) solar cells. However, for many years researchers realized that in some specific situations solar dynamic power systems with thermal energy storage can provide significant savings in life cycle costs and launch mass when compared with conventional photovoltaic power systems with battery storage [3–6]. A standard solar dynamic power system uses a mirror to concentrate solar radiation onto an absorber structure. By conduction through a solid material or circulation of a working fluid, the absorber heat is transferred to a thermal converter (i.e., a turbogenerator, Stirling engine, thermocouple or thermionic-emitter). For continuous operation during dark periods the use of melted materials to store thermal energy is being considered. Among the advantages of dynamic power systems one could quote their ability to provide electrical energy and heat simultaneously, the fact that the power plant may be unified by using either solar or nuclear energy or their relative invulnerability to corpuscular particles and to electromagnetic radiation [5]. A comparison between the various power systems designed for the Space Station Freedom shows the sun-to-user efficiency is 5.7–6.8% for the PV system and 18.7–19.8% for the dynamic system. If, in addition, the storage subsystem is taken into consideration, the solar dynamic system becomes even more attractive, mainly because the efficiency of the latent heat storage is higher compared to the Ni–Cd batteries of the PV system (for details see [7]).

In this paper we propose a model of dynamic solar power plant operating on the surface of Mars. A number of power systems were already designed to be used under the Martian environment but all of them are based on photovoltaics. Indeed, PV cells are envisaged to power small rovers [8], long-endurance, remotely piloted aircraft capable of flight within the Martian environment [9] and to ensure the life support for a 40 day manned Mars surface scientific expedition [10]. More recently, the Sojourner of the Pathfinder mission was also powered by PV cells (see e.g. [11]). Our most important question is: are properly designed dynamic systems comparable in performance with the PV-based power systems? Some of the references we have already cited seem to indicate an affirmative answer. However, they all refer to systems operating in the interplanetary space. A surface-based power system has to take into consideration one very important feature of the Martian weather. The period between the areocentric longitude $L_s = 161–326^\circ$E and variants thereof have been referred to as the ''dust storm season''. This period is nearly centered on perihelion, which is the time of

maximum insolation on Mars [12,13]. In the northern hemisphere, the Martian atmosphere varies greatly from year to year during the dust storm season, while at the other seasons most phenomena are remarkably similar from year to year. Zurek et al. [14] provide the most comprehensive description of Martian meteorology.

The dust storm periods are characterized by an almost vanishing direct solar radiation (see e.g. [15] and references therein). The main consequence is that diffuse solar radiation cannot be concentrated and *flat-plate* solar collectors have to be used in this case. But common Earth practice proved that very low efficiency is associated with solar power generation using flat-plate (blackbody-like) collectors. The model we develop here is based on flat-plate *selective* solar collectors, which are operating at higher efficiency.

Previous practice proved that three different cycles could be used for thermodynamic conversion of solar radiation: Brayton, Rankine and Stirling [3,5]. To provide an upper limit for the performance of an actual thermal engine we shall use here a Carnot endoreversible cycle. This has, on one hand, the advantage of generality and, on the other hand, it takes into account the irreversibilities associated to the heat transfer at the hot and cold parts of the engine.

2. Solar power plant model

Generally, a solar power plant consists of a solar collector, a thermal engine and a heat storage system. A solar collector mainly consists of mirror, absorber (receiver), transparent cover(s) and thermal insulation. The mirror is missing in the case of flat-plate collectors, while for some concentration systems the receiver is not protected by transparent cover(s).

Direct beam (b), diffuse (d) and ground reflected (r) fluxes of solar energy are incident on the collector. Their magnitude depends upon the collector's tilt and orientation. Generally, the incident and absorbed solar energy density fluxes (φ_{inc} and φ_{abs}, respectively), are given by

$$\varphi_{inc} = G_b + G_d + G_r \tag{1}$$

$$\varphi_{abs} = \rho_m C(\tau\alpha)_b G_b + (\tau\alpha)_d (G_d + G_r) \tag{2}$$

Here G denote solar irradiances at collector level, ρ_m — mirror's reflectance, C — concentration ratio while $(\tau\alpha)$ are effective transmittance–absorptance products.

The solar power plant analyzed in this paper is designed to operate during the whole Martian year. Consequently, it consists of a *flat-plate* selective solar collector coupled to a thermal engine. No heat storage system is considered in this approach. One denotes by T_C and T_a the collector and ambient temperatures, respectively.

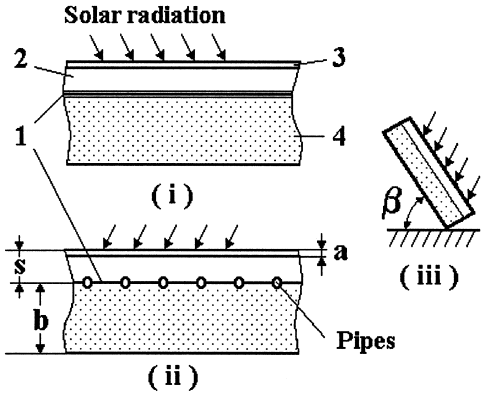

Fig. 1. Solar collector: (i) longitudinal section; (ii) transversal section; (iii) lateral view. 1 — absorber plate; 2 — carbon dioxide layer; 3 — transparent cover; 4 — bottom thermal insulation.

2.1. Solar collector model

A selective flat-plate solar collector is shown in Fig. 1. Its main components are: the absorber plate (1) with pipes for the working fluid and a transparent cover (3) of thickness a. The gap between (1) and (3) (thickness s) is filled with carbon dioxide at the Martian atmospheric pressure (carbon dioxide represents 95% of the Martian atmosphere). The bottom thermal insulation (4) has a thickness b. The collector tilt angle is β. Various temperatures related to collector operation are defined in Table 1.

The collector heat losses will be studied by using the thermal resistance method [2] (see Fig. 2 and Table 2). Then, the flux of heat losses from the collector towards the ambient is given by:

$$q_{\mathrm{tot}} = U_{\mathrm{L}}(T_{\mathrm{C}} - T_{\mathrm{a}}) = (T_{\mathrm{C}} - T_{\mathrm{a}})/R_{\mathrm{tot}} \tag{3}$$

Table 1
Various temperatures related to collector operation

Temperatures	
T_{C}	Absorber plate temperature
T_{si}	Temperature of lower surface of transparent cover
T_{ss}	Temperature of higher surface of transparent cover
T_{a}	Atmosphere temperature
Average temperatures	
$T_{\mathrm{C,si}} = (T_{\mathrm{C}} + T_{\mathrm{si}})/2$	Average fluid temperature between absorber plate and lower surface of transparent cover (see Fig. 2)
$T_{\mathrm{s}} = (T_{\mathrm{si}} + T_{\mathrm{ss}})/2$	Average transparent cover temperature
$T_{\mathrm{ss,a}} = (T_{\mathrm{ss}} + T_{\mathrm{a}})/2$	Average temperature of the atmosphere boundary layer near the collector transparent cover
$T_{iz} = (T_{\mathrm{C}} + T_{\mathrm{a}})/2$	Average bottom insulation temperature

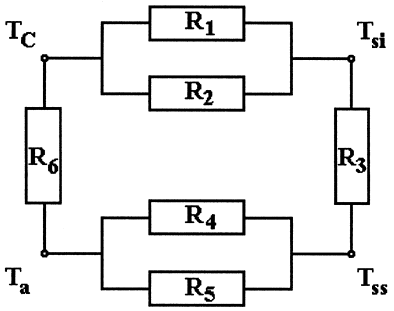

Fig. 2. Solar collector thermal resistances. T_a — ambient temperature; T_C — absorber plate temperature; T_{si} — temperature of lower surface of transparent cover; T_{ss} — temperature of higher surface of transparent cover.

where U_L is the overall heat losses coefficient while R_{tot} is the total thermal resistance. U_L is given by (see Fig. 2):

$$U_L = \frac{1}{R_{tot}} = \frac{1}{R_{1-5}} + \frac{1}{R_6} \tag{4}$$

where R_{1-5} is computed from:

$$R_{1-5} = \frac{R_1 R_2}{R_1 + R_2} + R_3 + \frac{R_4 R_5}{R_4 + R_5} \tag{5}$$

Details concerning the evaluation of thermal resistances follow. The thermal resistance R_1 is computed from:

$$R_1 = \frac{s}{\langle \lambda_{CO_2} \rangle_{C,si} Nu_{C,si}} \tag{6}$$

Table 2
Thermal resistances associated to solar collector operation (see Figs. 1 and 2)

Thermal resistance	Process
R_1	Convection and conduction between the absorbent plate (1) and the transparent cover (3)
R_2	Radiation between the absorbent plate (1) and the lower surface of the transparent cover (3)
R_3	Conduction through the transparent cover (3)
R_4	Radiation between the higher surface of the transparent cover (3) and Martian atmosphere
R_5	Convection between the higher surface of the transparent cover (3) and Martian atmosphere
R_6	Conduction through the bottom thermal insulation (4)

Table 3
Relationships for convection heat transfer between: (a) absorber plate and transparent cover [16]. 'H' and 'V' denote a horizontal and vertical solar collector; β [rad] and L are tilt angle and collector length, respectively; (b) two plane parallel surfaces [17, p. 160]

(a)	$Nu_{C},si=[1-(\beta/2\pi)]Nu_{H}+(\beta/2\pi)Nu_{V}$
$Nu_{H}=0.195Gr^{0.25}$	For $2\times10^{3}\le Gr<4\times10^{5}$
$Nu_{H}=0.068Gr^{0.33}$	For $Gr\ge4\times10^{5}$
$Nu_{V}=0.180Gr^{0.25}(s/L)^{0.11}$	For $1\times10^{4}\le Gr<2\times10^{5}$
$Nu_{V}=0.065Gr^{0.33}(s/L)^{0.11}$	For $2\times10^{5}\le Gr<11\times10^{6}$

(b)	
$Nu_{C,si}=1$	For $Gr\ Pr\le1\times10^{3}$
$Nu_{C,si}=0.105(Gr\ Pr)^{0.30}$	For $1\times10^{3}<Gr\ Pr\le1\times10^{6}$
$Nu_{C,si}=0.400(Gr\ Pr)^{0.20}$	For $1\times10^{4}\le Gr<2\times10^{5}$
$Nu_{C,si}=0.180(Gr\ Pr)^{0.25}$	For $Gr\ Pr>1\times10^{10}$

where $\langle\lambda_{CO_2}\rangle_{C,si}$ is the thermal conductivity of carbon dioxide and $Nu_{C,si}$ is the Nusselt number, both of them evaluated at the average fluid temperature $T_{C,si}$. To compute $Nu_{C,si}$, a number of criterial relationships developed for solar collectors were used [16] (Table 3a). For cases not covered by Table 3a, we used the general equations from [17] (Table 3b).

Prandtl and Grashoff numbers in Table 3a,b were computed with:

$$Pr=\frac{\langle c_{p,\,CO_2}\rangle_{C,si}\langle\eta_{CO_2}\rangle_{C,si}}{\langle\lambda_{CO_2}\rangle_{C,si}};\quad Gr=\frac{g_M p_{CO_2}^2 s^3(T_C-T_{si})}{\langle\eta_{CO_2}\rangle_{C,si}R_{CO_2}T_{C,si}} \tag{7}$$

where g_M is gravitational acceleration on Mars, while p_{CO_2} and R_{CO_2} are the pressure and gas constant for the carbon dioxide between absorber plate and transparent cover. In (7) the specific heat at constant pressure ($\langle c_{p,CO_2}\rangle_{C,si}$), the dynamic viscosity ($\langle\eta_{CO_2}\rangle_{C,si}$) and the thermal conductivity ($\langle\lambda_{CO_2}\rangle_{C,si}$) of carbon dioxide were interpolated at the average temperature $T_{C,si}$. In computations, the thermal properties of carbon dioxide from [8] were used.

One neglects the radiation absorbtion in the thin carbon dioxide layer between absorber plate and transparent cover. The thermal resistance R_2 is then evaluated with:

$$R_2=\frac{1/\epsilon_1+1/\epsilon_2-1}{2\sigma(T_C^2+T_{si}^2)T_{C,si}} \tag{8}$$

where ϵ_1 and ϵ_2 are the global hemispherical emittance of absorber plate and lower surface of transparent cover, respectively [19] and σ is Boltzmann constant.

Table 4
Relationships for forced convection heat transfer between transparent cover and atmosphere [17, p. 126]

$X_T = 5 \times 10^5(\langle\eta_{CO_2}\rangle_{ss,a} R_{CO_2} T_{ss,a}/p_{CO_2} W)$	
$Nu_{ss,a} = 0.335\ Re^{0.50}\ Pr^{0.50}$	For $L \leq X_T$ (laminar flow)
$Nu_{ss,a} = 0.036\ Re^{0.80}\ Pr^{0.75}$	For $L > X_T$ (turbulent flow)

The thermal resistance R_3 is given by:

$$R_3 = a/\lambda_s \tag{9}$$

The temperature dependence of transparent cover's thermal conductivity (λ_s) was described by using an interpolation parabolic function whose coefficients were obtained by using experimental data (in application the transparent cover is made of light silicate flint glass (65% silica wt.); thermal properties are found in [20,28]). The average transparent cover temperature T_s was used in computations.

The thermal resistance R_4 was evaluated with:

$$R_4 = \frac{1/\epsilon_2}{2\sigma(T_{ss}^2 + T_a^2)T_{ss,a}} \tag{10}$$

where $T_{ss,a}$ is the average temperature of the atmosphere boundary layer near the collector transparent cover.

Because of wind, the heat transfer between the transparent cover and Martian atmosphere is mainly by forced convection. Thus, the thermal resistance R_5 was computed from:

$$R_5 = \frac{L}{\langle\lambda_{CO_2}\rangle_{ss,a} Nu_{ss,a}} \tag{11}$$

where L is collector's length on wind direction and $\langle\lambda_{CO_2}\rangle_{ss,a}$ is carbon dioxide thermal conductivity at temperature $T_{ss,a}$. In (11) $Nu_{ss,a}$ depends on the critical length X_T which separates the laminar and turbulent wind flows over the collector. The relationships from Table 4 were used. In Table 4 the Reynolds and Prandtl numbers were evaluated with:

$$Re = \frac{P_{CO_2} WL}{\langle\eta_{CO_2}\rangle_{ss,a} R_{CO_2} T_{ss,a}}; \quad Pr = \frac{\langle c_{p,CO_2}\rangle_{ss,a}\langle\eta_{CO_2}\rangle_{ss,a}}{\langle\lambda_{CO_2}\rangle_{ss,a}} \tag{12}$$

where W is wind speed and the thermal properties of the atmosphere ($\langle\eta_{CO_2}\rangle_{ss,a}$, $\langle c_{p,\,CO_2}\rangle_{ss,a}$ and $\langle\lambda_{CO_2}\rangle_{ss,a}$) were interpolated at the average temperature $T_{ss,a}$. In applications thermal properties of carbon dioxide from [18] were used.

The thermal resistance R_6 was evaluated with:

$$R_6 = b/\lambda_{iz} \tag{13}$$

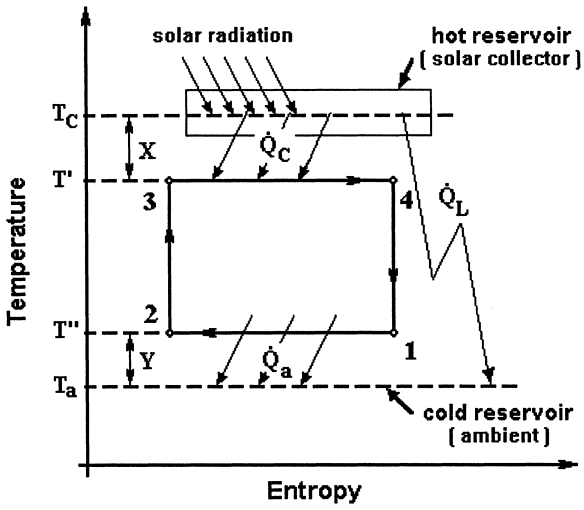

Fig. 3. Temperature — entropy diagram for an endoreversible Carnot cycle (for notations see text).

where λ_{iz} is bottom insulation thermal conductivity, computed at the average temperature T_{iz}.

2.2. Thermal engine model

A variety of working fluids were proposed to be used in space solar engines. They include mercury, potassium and rubidium in the early studies [3] or organic fluids and mixtures of noble gases more recently [2,4]. The latter seem to be more appropriate in the case of Martian solar power plants. The largest and smallest working fluid temperatures are denoted T' and T'', respectively (Fig. 3). Generally, $T_C > T'$ and $T'' > T_a$. Hence, both

$$X \equiv T_C - T' \quad \text{and} \quad Y \equiv T'' - T_a \tag{14}$$

are positive quantities.

The flux of solar energy ϕ_{abs} absorbed by the collector is

$$\phi_{abs} = \varphi_{abs} A_C \tag{15}$$

where A_C is the collector surface area, while φ_{abs} is the absorbed energy density flux.

Part of this flux is transferred to the working fluid ($\dot{Q}_C$) while the other part constitutes the flux of thermal losses to the ambient ($\dot{Q}_L$). Then, the solar collector steady-state energy balance is:

$$\phi_{abs} - \dot{Q}_C - \dot{Q}_L = 0 \tag{16}$$

The heat fluxes $\dot{Q}_C$ and $\dot{Q}_L$ can be written as:

$$\dot{Q}_C = h_C A_C X \quad \text{and} \quad \dot{Q}_L = U_L A_C (T_C - T_a) \tag{17}$$

where h_C and U_L are appropriately defined overall heat transfer coefficients between the solar collector and the working fluid and ambient, respectively.

The Carnot engine partially converts the flux $\dot{Q}_C$ into power. Thus:

$$\dot{Q}_C = \dot{W} + \dot{Q}_a \tag{18}$$

where $\dot{W}$ is the output power and $\dot{Q}_a$ is the thermal energy flux finally reaching the surroundings. There is no further increase of entropy during work production. Consequently

$$\frac{\dot{Q}_C}{T'} + \frac{\dot{Q}_a}{T''} = 0 \tag{19}$$

The heat flux $\dot{Q}_a$ can be written as

$$\dot{Q}_a = h_a A_a Y \tag{20}$$

where A_a and h_a are appropriately defined engine's radiator heat transfer area and overall heat transfer coefficient between working fluid and ambient, respectively.

2.3. Performance indicators

Two performance indicators were considered in this work. First, there is the output power $\dot{W}$, evaluated from:

$$\dot{W} = h_C A_C X - h_a A_a Y \tag{21}$$

Here we used the Eqs. (17), (18) and (20).

Second, there is the solar (or sun-to-user) efficiency defined as:

$$\eta_{solar} \equiv \frac{\dot{W}}{\phi_{inc} A_C} \tag{22}$$

with $\phi_{inc} = \varphi_{inc} A_C$.

Other indicators as the Carnot engine efficiency could also be used.

2.4. Optimization

The output power $\dot{W}$ will be maximised here. The weight of space power plants should be kept at minimum. Following previous studies (see e.g. [21]), we express the mass of the *total* heat transfer area (i.e. the mass M_C of the solar collector and the mass M_a of the engine's radiator) as a k fraction from the total mass M_{tot} of the space system:

$$M_C + M_a = k M_{tot} \tag{23}$$

One denotes d_C and d_a the superficial mass density of collector and radiator, respectively. One can simply write:

$$M_C = d_C A_C; \quad \text{and} \quad M_a = d_a A_a \tag{24}$$

One can use $d_C = d_a$ as a reasonable assumption. By using Eqs. (23) and (24) one derives the following constraint to be fulfilled:

$$A_C + A_a = A \equiv k\frac{M_{tot}}{d_a} \tag{25}$$

Other constraints (say F_1 and F_2) are the Eqs. (16) and (19). By using (14), (17) and (20) they become:

$$F_1 \equiv \frac{h_C A_C X}{T_C - X} - \frac{h_a(A - A_C)}{T_a + Y} = 0 \tag{26}$$

$$F_2 \equiv \varphi_{abs} - U_L(T_C - T_a) - h_C X = 0 \tag{27}$$

The power $\dot{W}$ is considered here as a function of T_C, X, Y and A_C. The Lagrange function L associated to $\dot{W}$ is:

$$L \equiv \dot{W} + \lambda_1 F_1 + \lambda_2 F_2 \tag{28}$$

where λ_1 and λ_2 are multipliers.

The maximum output power is obtained by solving the six equations shown in Table 5. Table 6 shows the solution, which applies for $K > 1$. There, the dimensionless parameters K and f are defined as:

$$K \equiv \frac{h_a}{h_C}\left(1 + \frac{h_C}{U_L}\right); \quad f = \frac{\varphi_{abs}}{U_L T_a} \tag{29}$$

Table 5
Equations to be solved for power maximization (for details see text)

1. $\frac{\partial L}{\partial T_C} = -\lambda_1 \frac{h_C A_C X}{(T_C - X)^2} - \lambda_2 U_L = 0$
2. $\frac{\partial L}{\partial X} = h_C A_C + \lambda_1 \frac{h_C A_C T_C}{(T_C - X)^2} - \lambda_2 h_C = 0$
3. $\frac{\partial L}{\partial Y} = -h_a(A - A_C) - \lambda_1 \frac{h_a(A - A_C) T_a}{(T_a + Y)^2} = 0$
4. $\frac{\partial L}{\partial A_C} = h_C X + h_a Y + \lambda_1 [\frac{h_C}{T_C - X} + \frac{h_a Y}{T_a - Y}] = 0$
5. $\frac{\partial L}{\partial \lambda_1} = \frac{h_C A_C X}{T_C - X} - \frac{h_a(A - A_C) Y}{T_a + Y} = 0$
6. $\frac{\partial L}{\partial \lambda_2} = \varphi_{abs} - U_L(T_C - T_a) - h_C X = 0$

Table 6
Optimum parameters for maximum output power (for details see text)

1. $T_{C,opt} = [1 + f - \frac{1+f-(1+f)^{1/2}}{K^{1/2}(1+K^{1/2})} \frac{h_a}{U_L}]T_a$
2. $X_{opt} = \frac{(1+f)-(1+f)^{1/2}}{K^{1/2}(1+K^{1/2})} \frac{h_a}{h_C} T_a$
3. $Y_{opt} = \frac{(1+f)^{1/2}-1}{1+K^{1/2}} T_a$
4. $A_{C,opt} = \frac{K^{1/2}}{1+K^{1/2}} A$

Table 6 and Eq. (21) allow to write the maximum power as:

$$\dot{W}_{max} = \frac{h_a A}{T_a} Y_{opt}^2 \tag{30}$$

The optimum solar efficiency $\eta_{solar,opt}$ can be derived by using Eqs. (22), (30) and Table 6.

3. Meteorologic and actinometric data

During the application we used as input data, values of ambient pressure and temperature, wind speed and atmospheric optical depth measured at Viking Lander 1 (VL1) (22.3°N, 47.9°W) and Viking Lander 2 (VL2) (47.7°N, 225.7°W) sites. The data were taken from the Viking Lander Meteorology and Atmospheric Opacity Data Set Archive from the Planetary Data System database made publically available on a compact disc [22]. Three electronic files were used here, namely VL_MBIN.DAT and VL_TBIN.DAT (which contain values of atmospheric pressure and temperature and zonal and meridional wind speed, among others) and VL_OPAC.DAT (which contains atmospheric optical depth data).

The file VL_MBIN.DAT (8325 records) contains binned and splined data obtained from the Viking Meteorology Instrument System (VMIS) through portions of the Viking Lander 1 mission. The file VL_TBIN.DAT (25750 records) contains binned and splined data obtained from the VMIS through most of the Viking Lander 2 mission and the early days of the Lander 1 mission. In both cases the numbering of the Martian solar days (sols) started at day 0 when each Lander touched down. Both files VL_MBIN.DAT and VL_TBIN.DAT contain mean values of meteorological parameters in each bin. The bin number starts with 0 at local midnight and increments by 1 each 1/25 of a sol. The file VL_OPAC.DAT (1044 records) stores measurements of atmospheric optical depth and associated errors estimates. Each record contains the optical depth value and its associated local solar time (in Earth hours) beginning at midnight.

As the files VL_MBIN.DAT and VL_TBIN.DAT are more "dense" than the

VL_OPAC.DAT file, a time interpolation procedure was used to obtain the values of the atmospheric pressure and temperature and wind velocity associated to a given record of atmospheric optical depth (for details see [23]). The atmospheric pressure values are missing for eleven records. In these cases the following procedure was adopted:

1. In the case of the record VL2, year 1, areocentric longitude = 229.808 (autumn), sol = 200, hour = 11.41, we used the arithmetic mean of the pressure values corresponding to sol = 199, hour = 13.87 and sol = 201, hour = 11.42, respectively.
2. In the case of the record VL2, year 2, areocentric longitude = 19.228 (spring), sol = 454, hour = 9.62, we used the arithmetic mean of the pressure values corresponding to sol = 453, hour = 17.33 and sol = 454, hour = 17.25, respectively.
3. In the case of VL2, year 2, the first nine records during summer (areocentric longitudes between 93.363 and 100.510) we used the pressure value corresponding to the tenth record (areocentric longitude = 101.697, sol = 634, hour = 6.98).

A set of *complete* records was finally obtained. Each complete record associates to a given sol number and a local solar time value a set of four meteorological values, namely optical depth τ *and* atmospheric temperature T_a, atmospheric pressure p_a and wind speed W. The number of complete records is rather small (Table 7).

The optical depth values were used to evaluate the incoming fluxes of solar radiation. The resulting file of solar energy data was used as input during the simulation of solar heat engine operation. The three components of global radiation flux (namely direct, diffuse and ground reflected) were computed by

Table 7
The number of *complete* records used during simulations of solar dynamic power system operation

		Viking Lander 1		Viking Lander 2	
		Sol numbers	Number of complete records	Sol numbers	Number of complete records
Year 1	Spring	–	–	–	–
	Summer	6–155	22	6–111	37
	Autumn	168–306	108	120–257	77
	Winter	307–350	56	269–415	55
Year 2	Spring	–	–	416–608	147
	Summer	–	–	610–784	58
	Autumn	–	–	792–872	25
	Winter	–	–	–	–

using the procedure we previously proposed in [15]. The incoming fluxes of solar radiation were evaluated for all the complete records of Table 7.

4. Results and discussions

Four strategies of collecting solar energy were considered in a preliminary test [24]. The following two strategies will be used in this study: (i) horizontal collector — strategy H; (ii) the collector tilt and orientation are continuously adjusted to keep the receiving surface perpendicular on Sun's rays — strategy P. Strategy H is easier to use while strategy P gives the higher power output most times of the year.

A number of assumptions were accepted during model application. First, a simple relation is used for the two effective transmittance–absorptance products:

$$(\tau\alpha)_b = (\tau\alpha)_d = \tau_{cs}\alpha_{ps} \tag{31}$$

where τ_{cs} and α_{ps} are the transparent cover transmittance and absorber absorptance, respectively, both of them for short (solar) wavelengths.

Details about solar collector design are given in Table 8. Transparent cover's thermal conductivity lies between 0.691 W/mK at -100°C and 1.025 W/mK at $+100^{\circ}$C [20].

In order to allow comparison with PV power systems one can imagine a dynamic power system used on Mars Pathfinder's Sojourner. Sojourner was a small (11.5 kg), six-wheel robotic vehicle powered by a PV array weighting 0.34 kg [11]. Its photovoltaic cells were designed to provide 16 W of electric power at the noon of a clear summer Martian day. The ratio $0.34/11.5 = 0.0296$ can be used as a first estimate for the coefficient k to be used in Eq. (25). Preliminary tests were performed to determine an optimum collector area $A_{C,opt}$ close to Sojourner PV cell surface area (0.22 m^2). Finally, the value $A = 0.23$ m^2 was used in computations. It corresponds to a radiator superficial mass density $d_a = 1.48$ kg/m^2

Table 8
Details about selective flat-plate solar collector design

Quantity	Notation	Value
Concentration ratio	C	1
Number of transparent covers	N	1
Transparent cover thickness	a	0.003 m
Distance between transparent cover and absorber plate	s	0.045 m
Bottom thermal insulation thickness	b	0.1 m
Short wavelengths transparent cover transmittance	τ_{cs}	0.82
Short wavelength transparent cover absorptance	α_{ps}	0.90
Long wavelengths (IR) absorber plate emittance	ϵ_1	0.10
Long wavelengths (IR) transparent cover emittance	ϵ_2	0.88
Thermal conductivity of bottom insulation (polyurethane)	λ_b	0.02 W/m K

Table 9
Three design solutions for the system solar collector-thermal engine (h_a = heat transfer coefficient between the working fluid passing through the radiator of the heat engine and ambient [see Eq. (20)]; h_C = heat transfer coefficient between solar collector and working fluid [see Eq. (17)])

Case	h_a W/m^2 K	h_C W/m^2 K	Performance level
a	1	1	Low
b	10	10	Medium
c	500	50	High

in Eq. (25). It is rather close to the value $d_a = 2.3$ kg/m^2 accepted in [25] in the case of the radiator of a nuclear power satellite but only half of the value $d_a = 3$ kg/m^2 accepted in [26] for a solar power station. One could imagine technical solutions decreasing the radiator thickness but keeping its mechanical rigidity (for instance, by using fins).

4.1. Solar collector operation

The solar collector thermal losses mainly depend on the heat transfer regime between absorber plate and transparent cover (separated through the layer 2 of thickness s in Fig. 1). We considered the case of a flat plate horizontal solar collector (i.e. concentration ratio $C = 1$). Three design solutions were analyzed (Table 9). They correspond to different performance levels. For analysis we have chosen the middle of a clear sky autumn sol, when the thermal losses are higher [sol 301 VL1, 14.04 local solar time (LST)].

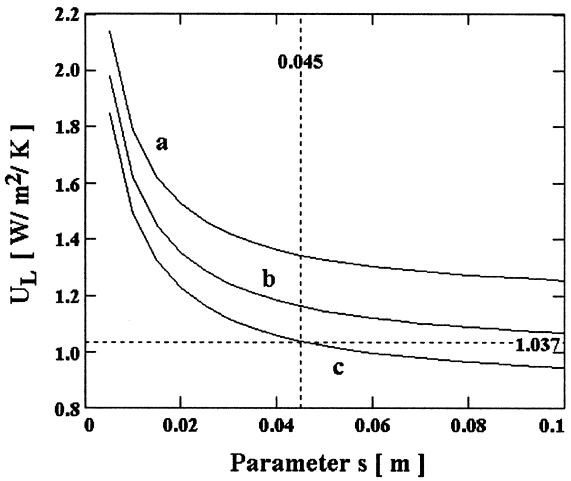

Fig. 4. Overall heat loss coefficient U_L as a function of parameter s (distance between absorber plate and transparent cover — see Fig. 1). Three-design solutions (a)–(c) were considered (see Table 9).

The dependence of the overall heat loss coefficient U_L on the distance s between absorber plate and transparent cover is shown in Fig. 4 for the three cases of Table 9. The heat losses decrease by increasing s. This is specific to the conduction heat transfer regime. The thickness s is limited, however, by economic reasons. In the following we use $s = 0.045$ m and the high performance design solution [case (c) in Table 9]. Note that the chosen value of s is about two times larger than the usual value for Earth placed solar collectors.

For Earth placed solar collectors the heat transfer between absorber plate and transparent cover is mainly by convection. This prompted various technical solutions meant to keep convection at local level (the honeycombs and Francia cells are examples of solutions for convection suppression (see [26] p. 404). The convective heat transfer is activated when the product $Gr\ Pr$ exceeds 1000 (see Table 7). We analyzed the heat transfer above the absorber plate by using the whole set of available meteorological data (Table 7).

The results show that the product $Gr\ Pr$ varies between 9.65 and 211.2, well below the threshold value of 1000. We draw the important conclusion that on Mars the thermal losses between absorber plate and transparent cover are by conduction and radiation with convection almost negligible.

The convection heat losses from transparent cover to atmosphere are mainly controlled by wind speed. The change from laminar to turbulent convection occurs in case the size of the heat transfer surface exceeds a certain critical length X_T (see Table 4). The flow regime above the transparent cover was analyzed by using the whole set of available meteorological data. Results are shown in Fig. 5. The minimum value of the critical length X_T is 5.43 m (Fig. 5(a)). Consequently, the convection heat transfer above the transparent cover is laminar. The critical length X_T is smaller during winter and larger during summer (Fig. 5(a)). No significant difference between VL1 and VL2 sites is observed (note that a larger number of meteorological values are available for VL2 — see Table 7). The critical length obviously decreases when the optical depth increases (Fig. 5(b)). During the "clear sky" days ($\tau < 1$) the critical length values have an important dispersion. Scattering diminishes during the dust storm days ($\tau > 1$).

For the design solution we selected, the values of the overall heat loss coefficient U_L range between about 0.5 and 1 W/m^2/K (Fig. 6). Broadly, these values are comparable with those of Earth located vacuum solar collectors (see e.g. [27], p. 387). The dispersion of the U_L values is slightly smaller during winter and higher during autumn (Fig. 6(a)). No obvious dependence of U_L on the optical depth is observed (Fig. 6(b)). However, the dispersion of the U_L values is larger for values $\tau < 1$, i.e. during the "clear" days. Also, Fig. 6 shows that U_L doesn't depend significantly on the latitude of the solar collector.

4.2. Thermal engine operation

An important influence on performance is induced by the parameters h_a and h_C. Again, a flat-plate solar collector ($C = 1$) with a total equivalent heat exchange area $A = 0.23$ m^2 in Eq. (25) was analyzed. We assumed $s = 0.045$ m. This value

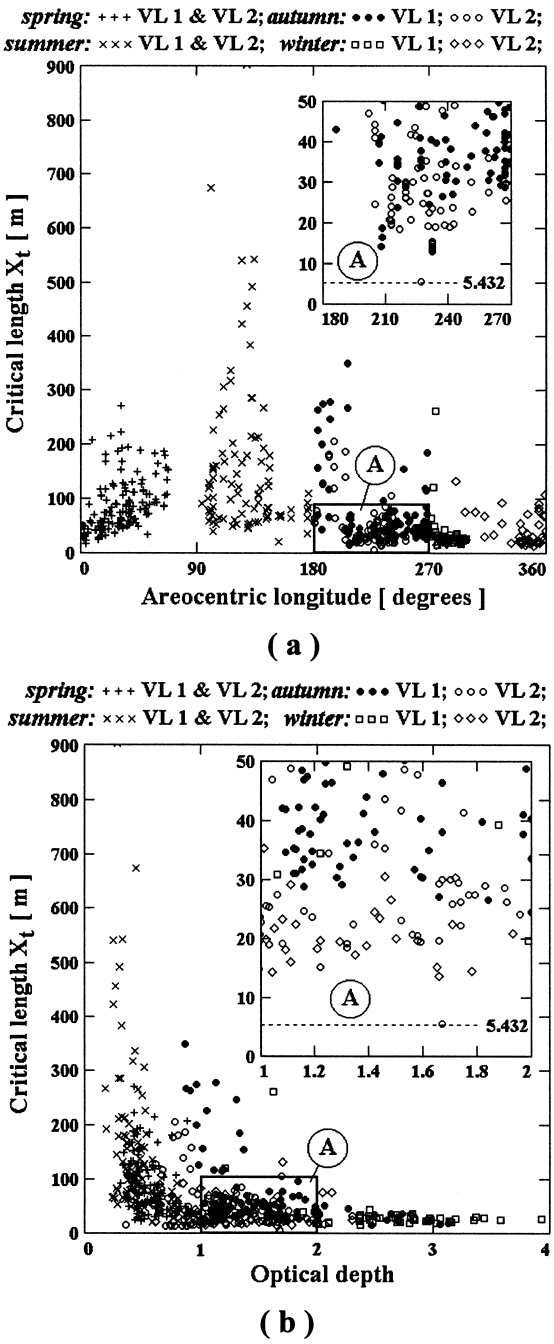

Fig. 5. Critical length X_T (see Table 4) as a function of (a) areocentric longitude and (b) optical depth. All available meteorological data were used. The design solution (c) of Table 9 was considered.

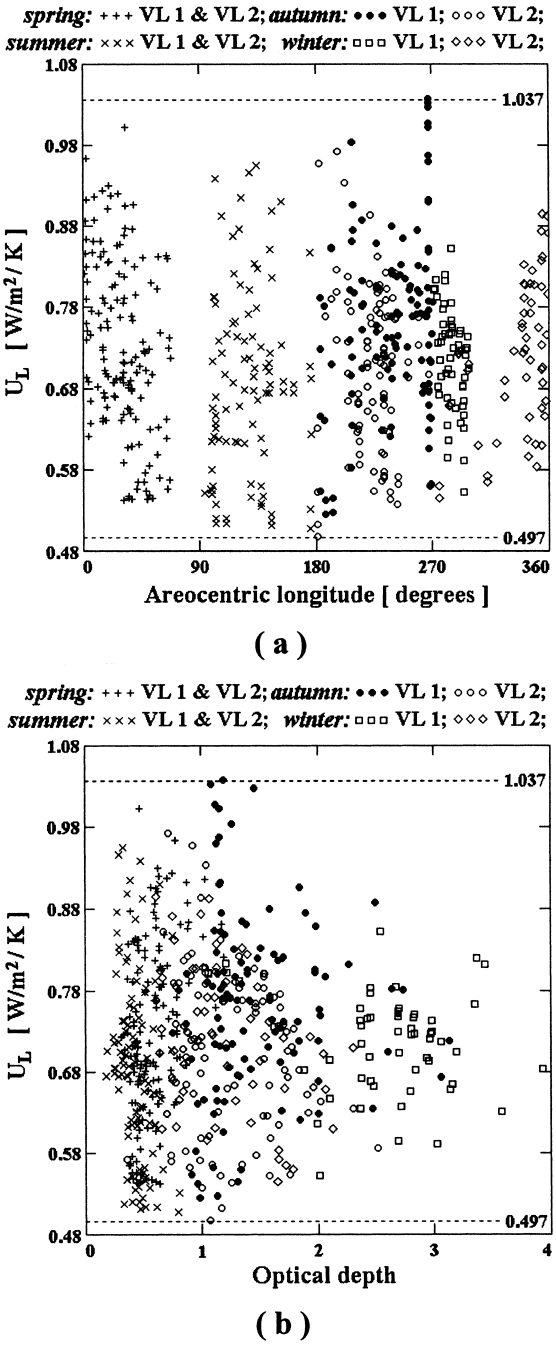

Fig. 6. Overall heat loss coefficient U_L as a function of (a) areocentric longitude and (b) optical depth. All available meteorological data were used. The design solution (c) of Table 9 was considered.

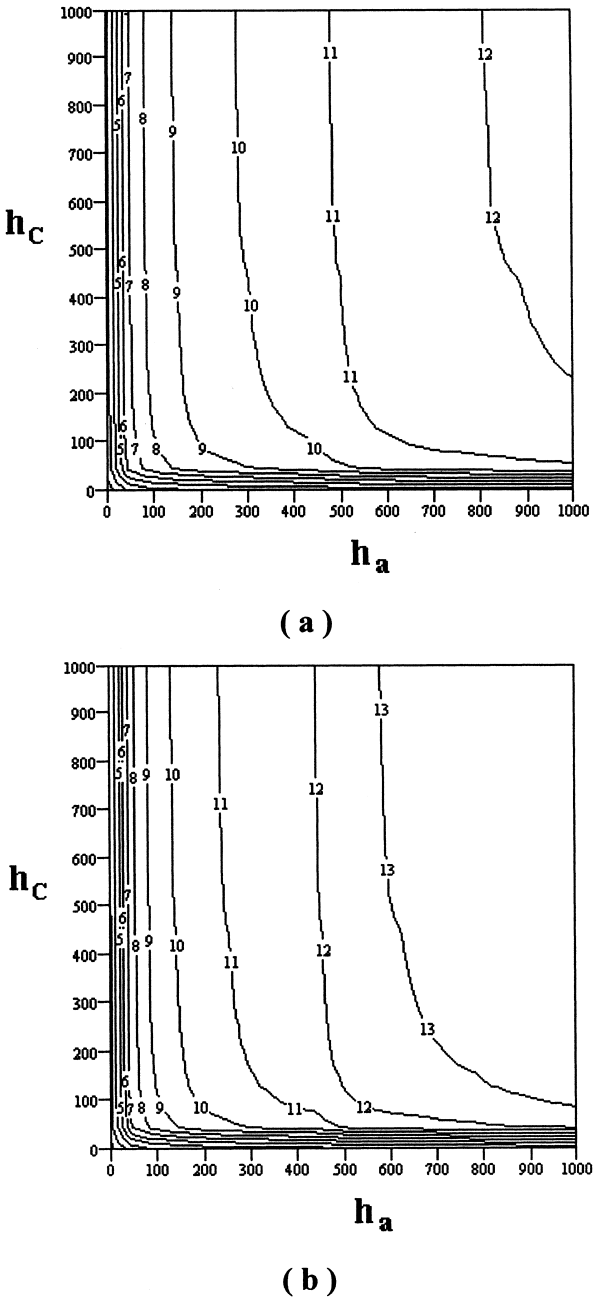

Fig. 7. Maximum power $\dot{W}_{max}$ provided by the thermal engine as a function of the overall heat transfer coefficients h_a and h_C. (a) horizontal solar collector (strategy H); (b) solar collector permanently perpendicular on the Sun's rays (strategy P). Unconcentrated solar radiation was considered (VL1, Autumn, sol 301, 14.04 LST).

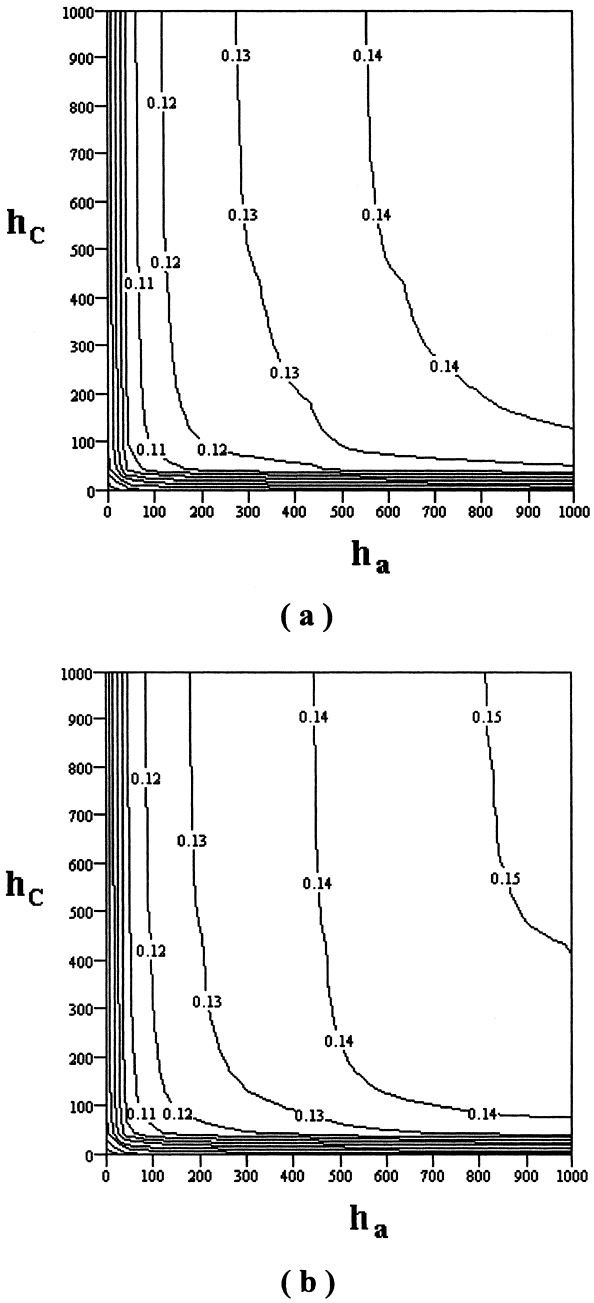

Fig. 8. Solar efficiency $\eta_{solar,opt}$ as a function of the overall heat transfer coefficients h_a and h_C. (a) horizontal solar collector (strategy H); (b) solar collector permanently perpendicular on the Sun's rays (strategy P). Unconcentrated solar radiation was considered (VL1, Autumn, sol 301, 14.04 LST).

is a compromise between a good thermal insulation and a reasonable size (see Fig. 4). For analysis we have chosen the middle of a clear sky autumn sol [sol 301 VL1, 14.04 local solar time (LST)]. Some results are shown in Figs. 7 and 8 for the maximum power provided by the thermal engine and the solar efficiency, respectively.

Generally, the influence on performance is strong for low values of both heat transfer coefficients h_a and h_C (less than 100 $W/m^2/K$). The performance is practically not dependent on the higher values of h_C. The influence of h_a on performance is more significant.

The strategies of collecting solar radiation have a rather weak influence on the dependence of performance on h_a and h_C (see Fig. 7(a) and (b), on the one hand, and Fig. 8(a) and (b), on the other hand). As expected, strategy *P* leads to higher performance.

The maximum output power could be as high as 12 W and 13 W in case of strategies *H* and *P* of collecting solar radiation, respectively. This is lower than the designed power of Sojourner's PV array (16 W at noon). However, this comparison put in disadvantage the solar dynamic system as we used input meteorological data from late autumn at VL1 site while Sojourner was designed to operate during Martian summer. This is a consequence of the fact that none of the 22 complete records available during summer at VL1 site (Table 7) corresponds to solar noon.

The influence of both h_a and h_C is more important on the maximum power provided by the heat engine than on the overall efficiency (compare, for instance, Figs. 7(a) and 8(a)).

5. Conclusions

The solar power plant analyzed in this paper is designed to operate during the whole Martian year. Consequently, it consists of a selective *flat-plate* solar collector coupled to a thermal engine operating on an endoreversible Carnot cycle. Methods of finite time thermodynamics are used to maximize the output power. During the optimization procedure the weight of the space power plant was used as a constraint.

During the application we used as input data values of atmospheric pressure and temperature, wind speed and atmospheric optical depth measured at Viking Landers sites.

The following two strategies of collecting solar energy were analyzed in this study: (i) horizontal collector — strategy *H*; (ii) the collector tilt and orientation are continuously adjusted to keep the receiving surface perpendicular on Sun's rays — strategy *P*.

The main results reported in this work are as follows.

1. The heat losses between the solar collector's absorber plate and transparent cover are by conduction and radiation. This differs from the Earth-based solar

collector where the main heat loss mechanism is convection.
2. The convection heat transfer above the transparent cover is laminar. This differs from the Earth-based solar collectors where turbulence is the main convection mechanism.
3. For the design solution we selected, the values of the overall heat loss coefficient U_L range between about 0.5 and 1 $W/m^2/K$. Roughly, these values are comparable with those of Earth located vacuum solar collectors. The dispersion of the U_L values is slightly smaller during winter and higher during autumn. No obvious dependence of U_L on the optical depth is observed. However, the dispersion of the U_L values is larger for values during the "clear" days. U_L doesn't depend significantly on the latitude of the solar collector.
4. Two parameters are used to quantify the heat transfer inside the thermal engine. They are h_a (=heat transfer coefficient between the working fluid passing through the radiator of the heat engine and ambient; see Eq. (20)) and h_C (=heat transfer coefficient between solar collector and working fluid [see Eq. (17)]). The influence of h_a on performance is more significant.
5. The strategy of collecting solar radiation has a rather weak influence on the dependence of performances on h_a and h_C. As expected, strategy P leads to higher performances.
6. The dynamic solar power plants equipped with selective flat-plate collectors could provide power comparable to that of PV cell systems.

References

[1] Aldrich AD. Mars: past, present and future. In: Pritchard EB, editor. Progress in astronautics and aeronautics, vol. 145. Washington: AIAA, 1992. p. 3–11.
[2] Angelino G, Invernizzi C. Cyclic Methylsiloxanes as working fluids for space power cycles. J Solar Energy Engng 1993;115:130–7.
[3] Menetrey WR. Space applications of solar energy. In: Zarem AM, Erway DD, editors. Introduction to the utilization of solar energy. New York: McGraw-Hill, 1963. p. 326.
[4] Prisnjakov VF, Statsenko IN, Kondratjev AI, Markov VL, Petrov BE, Gabrinets VA. Developing space power Brayton systems with solar heat input. In: Research of working process of high temperature latent heat storage system. Proceedings of the SPS 91, Power from Space, Paris, 27–30 August, 1991. p. 465–70.
[5] Prisnjakov VF. SPS interest and studies in USSR. In: Proceedings of the SPS 91, Power from Space, Paris, 27–30 August, 1991. p. 36.
[6] Secunde R, Labus TL, Lavely RG. Solar dynamic power module design. In: Proceedings of the 24th International Energy Conversion Conference, IEEE, Piscataway, NJ, 1989. vol. 1. p. 299–307.
[7] Weingartner S, Blumenberg J, Ruppe HO. Influence of orbit on solar–dynamic power systems. Space Power 1994;13(1 and 2):103–20.
[8] Hibbs BD. Mars rover feasibility study. Final Report Aero Vironement, Inc. Report AV-FR 89/7011, October 1989.
[9] Colloza AJ. Preliminary design of a long-endurance Mars aircraft, NASA CR185243, Sverdrup Technology Inc., Aerospace Technology Park, Brookpark, Ohio 44135. Prepared for Lewis Research Center under Contract NAS 3-25266, April 1990.

[10] McKissock BI, Kohout LL, Schmitz PC. A solar power system for an early Mars expedition. NASA Technical Memorandum 103219, Lewis Research Center, Cleveland, Ohio, American Institute of Chemical Engineers, Summer National Meeting, 19–23 August 1990.
[11] Golombek MP, Cook RA, Economou T, Folkner WM, Haldermann AFC, Kallemeyn PH, Knudsen JM, Manning RM, Moore HJ, Parker TK, Rider R, Schofield JT, Smith PH, Vaughan RM. Overview of the Mars Pathfinder mission and assessment of landing site predictions. Science 1997;278(5344):1743–8.
[12] Martin LJ, Zurek RW. An analysis of the history of dust activity on Mars. J Geophys Res 1993;98(E2):3221–46.
[13] Hourdin F, Forget F, Talagrand O. The sensitivity of the Martian surface pressure and atmospheric mass budget to various parameters: a comparison between numerical simulations and Viking observations. J Geophys Res 1995;100(E3):5501–23.
[14] Zurek RW, Barnes JR, Haberle RM, Pollack JB, Tillman JE, Leovy CB. Dynamics of the atmosphere Mars. In: Kieffer HH, editor. ''Mars''. Arizona: University of Arizona Press, 1992. p. 835–933 Chap. 26.
[15] Bădescu V. Different strategies for maximum solar radiation collection on Mars surface. Acta Astronautica 1998;43(7-8):409–21.
[16] Eaton CB, Blum HA. The use of moderate vacuum environments as a means of increasing the collectors efficiencies and operating temperatures of flat-plate solar collectors. Solar Energy 1975;17:151–8.
[17] Ştefănescu D, Marinescu M, Dănescu A. In: Transferul de caldură în tehnică, vol. 1. Bucureşti: Editura Tehnică, 1982.
[18] Pop MG, Leca A, Prisecaru I, Neaga C, Zidaru G, Muşatescu V, Isbăşoiu EC. In: Îndrumar — Tabele, monograme şi formule termotehnice, vol. 1. Bucureşti: Editura Tehnică, 1987.
[19] Duffie JA, Beckmann WA. Solar energy thermal processes. New York: Wiley, 1974.
[20] Lide David R, editor. Handbook of chemistry and physics, 71stth ed. C.R.C. Press, 1991. p. 15–39.
[21] Bădescu V. Dynamic solar space power systems: optimum design and operation. Space Technol 1994;14(5):331–7.
[22] Lee SW. Viking Lander Meteorology and Atmospheric Opacity Data Set Archive, Volume VL-1001. Laboratory for Atmospheric and Space Physics, Campus Box 392, University of Colorado, CO 80309-0392 1995.
[23] Bădescu V. Simulation of solar cells utilization on the surface of Mars. Acta Astronautica 1998;43(910):443–53.
[24] Bădescu V, Popescu G, Feidt M. Model of optimized solar heat engine operating on Mars. In: Bejan A, Fedit M, Moran MJ, Tsatsaronis G, editors. Proceedings of ECOS '98, Nancy, France, 8–10 July, 1998. vol. II. p. 813–9.
[25] Angelo JA, Buden Jr D. The nuclear power satellite (NPS) — key to a sustainable global energy economy and solar system civilization. In: Proceedings of SPS 91, Paris, 1991. p. 117–24.
[26] Mozjorine YA, Senkevich VP, Koval AD, Narimanov EA. Small-scale space power stations: feasibility and usage prospects. In: Proceedings of SPS 91, Paris, 1991. p. 381–92.
[27] Meinel AB, Meinel MP. Applied solar energy. Reading: Addison-Wesley, 1976.
[28] Lide David R, editor. Handbook of chemistry and physics, 71stth ed. C.R.C. Press, 1991. p. 331–7.